Supporting Information

Electrochemical engineering assessment of a novel 3D-printed filter-press electrochemical reactor for multipurpose laboratory applications

Raúl A. Márquez-Montes[1], Virginia H. Collins-Martínez[2], Ildebrando Pérez-Reyes[1], David Chávez-Flores[1], Olivia A. Graeve[3], and Víctor H. Ramos-Sánchez[1,3*]

[1] Facultad de Ciencias Químicas, Universidad Autónoma de Chihuahua, Nuevo Campus Universitario, Circuito Universitario, Chihuahua, Chih., C.P. 31125, México.

[2] Centro de Investigación en Materiales Avanzados, S.C., Miguel de Cervantes #120, Complejo Industrial Chihuahua, Chih., C.P. 31136, México.

[3] Department of Mechanical and Aerospace Engineering, University of California, San Diego, 9500 Gilman Drive - MC 0411, La Jolla, CA 92093, United States

* Corresponding author: vramos@uach.mx; vramossanchez@ucsd.edu

Number of pages: 22

Number of figures: 9

Number of tables: 4

1. Reactor components and diagrams

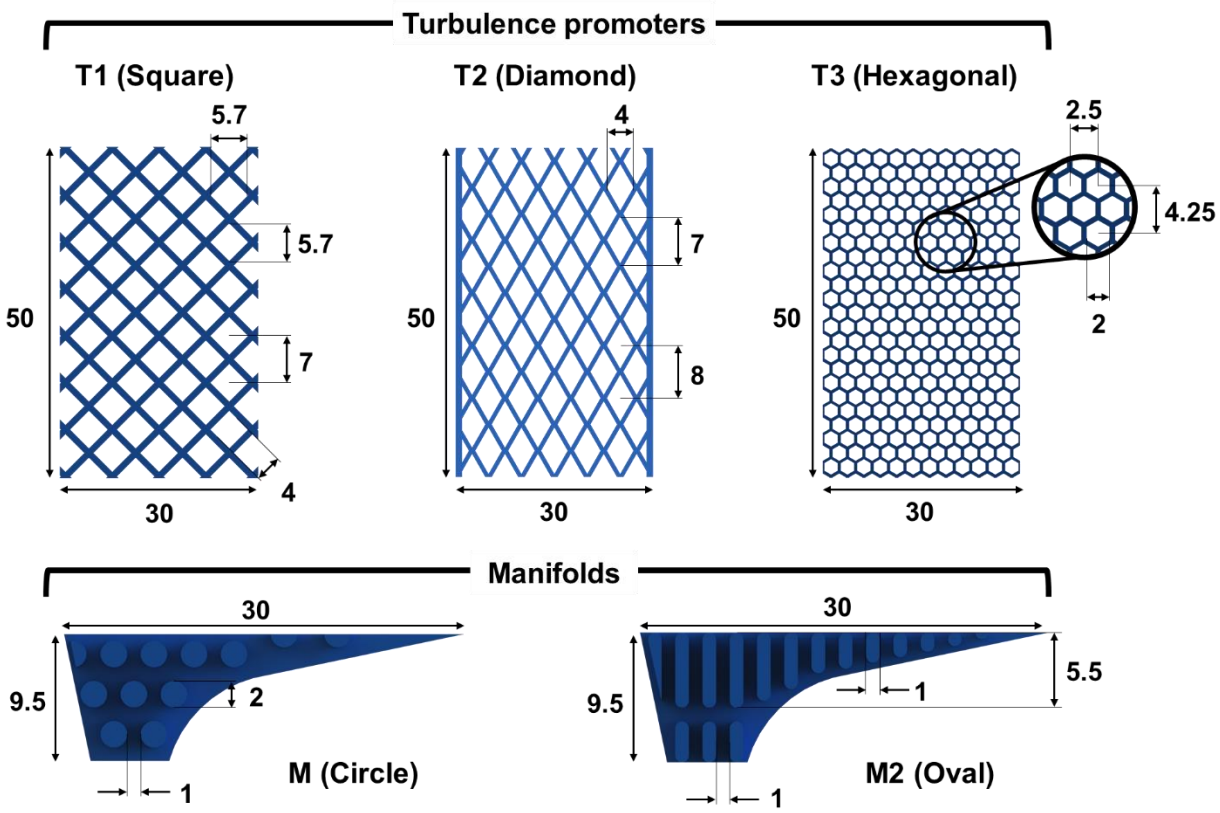

Figure S1. 3D-printed manifolds and turbulence promoters used in this study. Dimensions are given in mm.

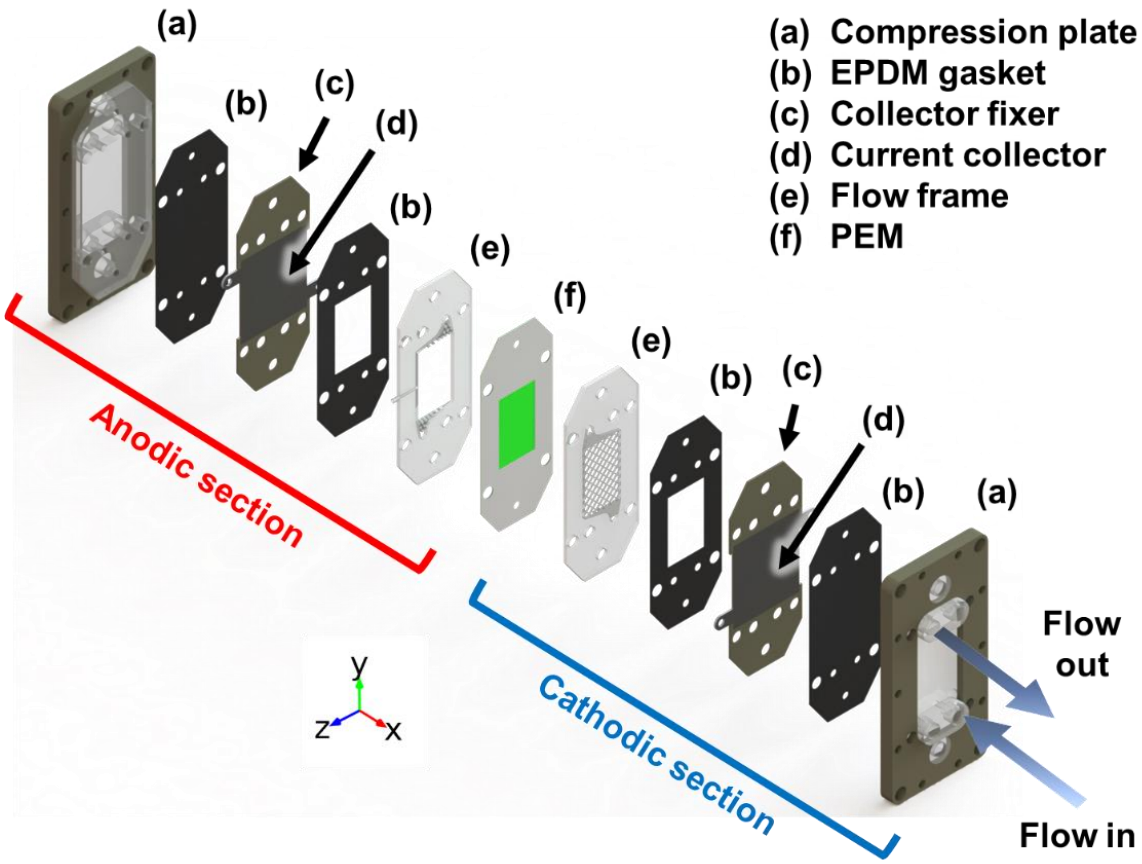

Figure S2. Electrochemical filter-press reactor assembly (one unit).

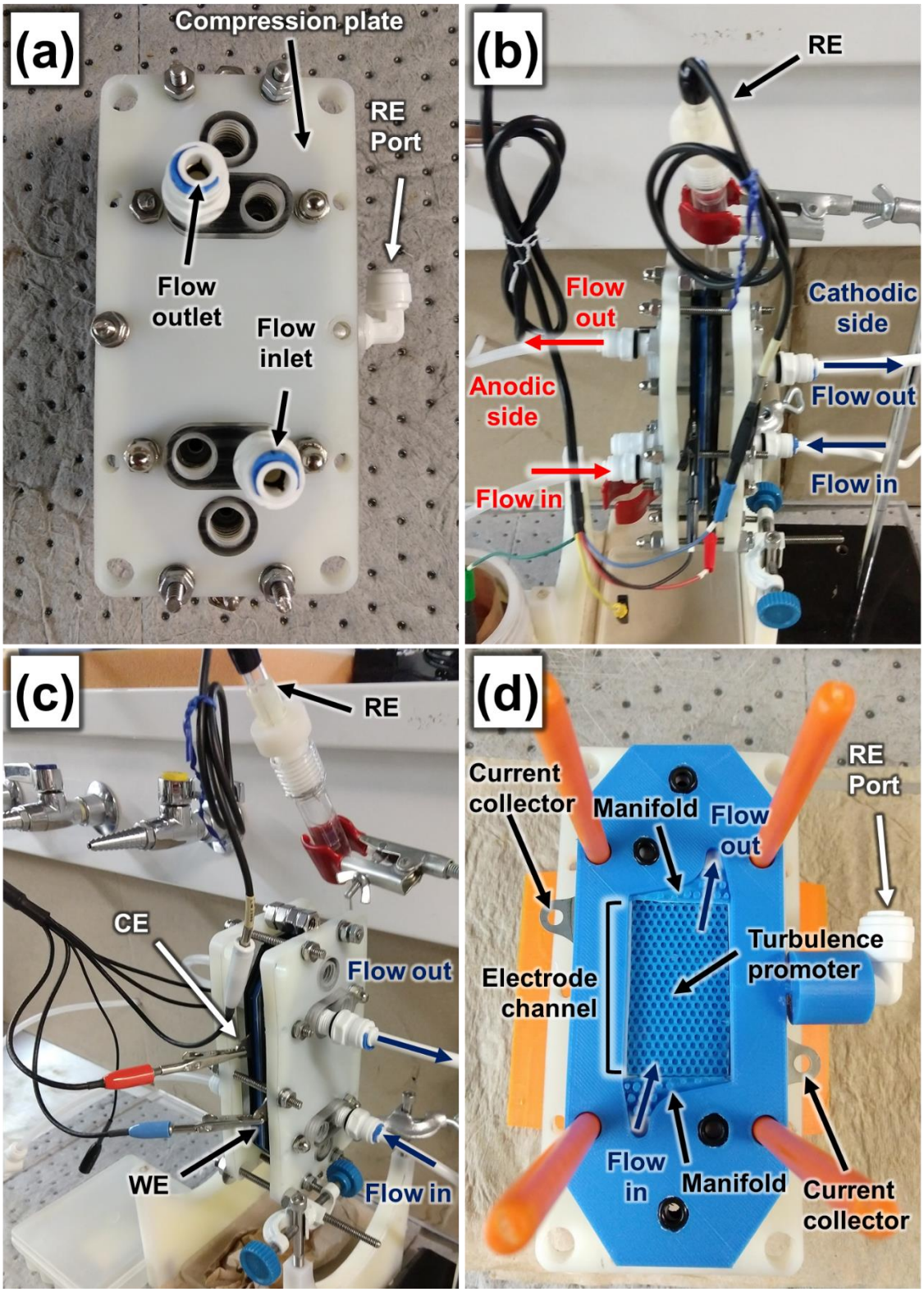

Figure S3. Digital photos of the electrochemical filter-press reactor: (a) front view of the cathodic side, (b) side-view of one-unit assembly, (c) close-up for better visualization of cell connections, (d) flow channel during cell assembly.

2. Ni Foam Cleaning Procedure.

Ni foam pieces (30 × 50 × 1.5 mm) were immersed in 50 mL of the following solutions while in an ultrasonic bath for 15 min each: (1) pure acetone, (2) 3 M HCl, (3) deionized water. Cleaned pieces were immediately loaded into the reactor and used in mass transfer studies. To reduce surface exposure to air, pieces were always kept immersed in degasified, deionized water until use.

3. Chemical Stability of 3D-printed Components.

Fresh test solutions were prepared using deionized water and analytical grade reagents, 97.5% or higher. Samples were immersed in vials filled with test solutions. Vials were stirred every 24 hours by moderate manual rotation. After one week of being immersed, samples were rinsed thoroughly with deionized water and left to dry in a desiccator for 24 hours at room temperature. Mass and size (*i.e.*, length and width/diameter) were measured before and after the tests, and relative difference percentages were calculated by means of eq S1:

$$\%D\delta = \frac{\left|\delta_i - \delta_f\right|}{\delta_i} \times 100 \qquad \text{(S1)}$$

where δ is the measured parameter and subscripts *i* and *f* refer to initial and final values, respectively. The following criterions were established to assess chemical stability: acceptable ($\Delta\delta \leq 1\%$), moderate ($1\% < \Delta\delta < 5\%$), and deficient ($\Delta\delta \geq 5\%$).

4. CFD Hydrodynamic Model.

The Reynolds-averaged Navier–Stokes (RANS) equations coupled with the standard k-ε turbulent model was selected since a non-ideal flow is expected due to the multi-sided geometries of manifolds and turbulence promoters, as it has been previously reported on comparable Reynolds numbers.[1] The hydrodynamic model included the RANS and continuity equations as shown in eqs S2 and S3, respectively:

$$\rho(\mathbf{u}\cdot\nabla)\mathbf{u} = -\nabla pI + \nabla\cdot\left[(\mu+\mu_T)\left(\nabla\cdot\mathbf{u}+(\nabla\cdot\mathbf{u})^T\right)\right] \quad \text{(S2)}$$

$$\nabla\cdot(\rho\mathbf{u}) = 0 \quad \text{(S3)}$$

where **u** is the velocity vector, ρ is the fluid density, p is the reference pressure in terms of the identity vector, μ_T is the eddy or turbulent viscosity, and μ is the dynamic viscosity. The standard k-ε turbulence model was used to solve turbulent viscosity, as defined by the following set of equations:

$$\mu_T = \rho C_\mu \frac{k^2}{\varepsilon} \quad \text{(S4)}$$

$$\rho(\mathbf{u}\cdot\nabla)k = \nabla\cdot\left[\left(\mu+\frac{\mu_T}{\sigma_k}\right)\nabla k\right] + P_k - \rho\varepsilon \quad \text{(S5)}$$

$$\rho(\mathbf{u}\cdot\nabla)\varepsilon = \nabla\cdot\left[\left(\mu+\frac{\mu_T}{\sigma_\varepsilon}\right)\nabla\varepsilon\right] + C_{\varepsilon1}\frac{\varepsilon}{k}P_k - C_{\varepsilon2}\rho\frac{\varepsilon^2}{k} \quad \text{(S6)}$$

where k is the turbulent kinetic energy, ε is the turbulent energy dissipation rate, P_k is the energy production term and C_μ, σ_k, σ_ε, $C_{\varepsilon1}$, and $C_{\varepsilon2}$ are dimensionless coefficients of the k-ε turbulence model.[1-3] Values used are shown in Table S1 and were taken from similar studies.[1, 3] Additionally, an enhanced wall treatment was employed as it has been previously suggested.[1]

Table S1. Conditions and parameters set for CFD simulations.

Temperature	298.15 K
Fluid	Water
k-ε turbulence model constants:	
C_μ	0.09
σ_k	1.00
σ_ε	1.30
$C_{\varepsilon 1}$	1.44
$C_{\varepsilon 2}$	1.92

Finally, a series of boundary conditions were used to effectively solve the equations:[1, 2] (1) initial values of the turbulent kinetic energy k_0, and turbulent energy dissipation rate ε_0, were fixed at 0.005 $m^2\ s^{-2}$ and 0.005 $m^2\ s^{-3}$, respectively; (2) the normal inflow velocity at the inlet was set as $\mathbf{u} = -\mathbf{n}U_o$, where **n** is the unit normal vector and U_0 is the average velocity at the entrance of the reactor; (3) the normalized velocity component inside the logarithmic boundary layer u^+, at a distance y^+ from the wall, is described by $u^+ = 2.5 \ln y^+ + 5.5$, in which a value of 11.06 was fixed for y^+; (4) the normal stress is equal to the pressure at the outlet as given by:

$$\left[-pI + \left(m + m_T\right)\left(\nabla \cdot \mathbf{u} + \left(\nabla \cdot \mathbf{u}\right)^T\right)\right] \cdot \mathbf{n} = -P_o \cdot \mathbf{n} \qquad \text{(S7)}$$

where p_0 is the pressure at the exit, stating that the flow inside the computational domain guides the turbulent characteristic of every flow element outside the domain. The following additional plots are given as reference of CFD studies.

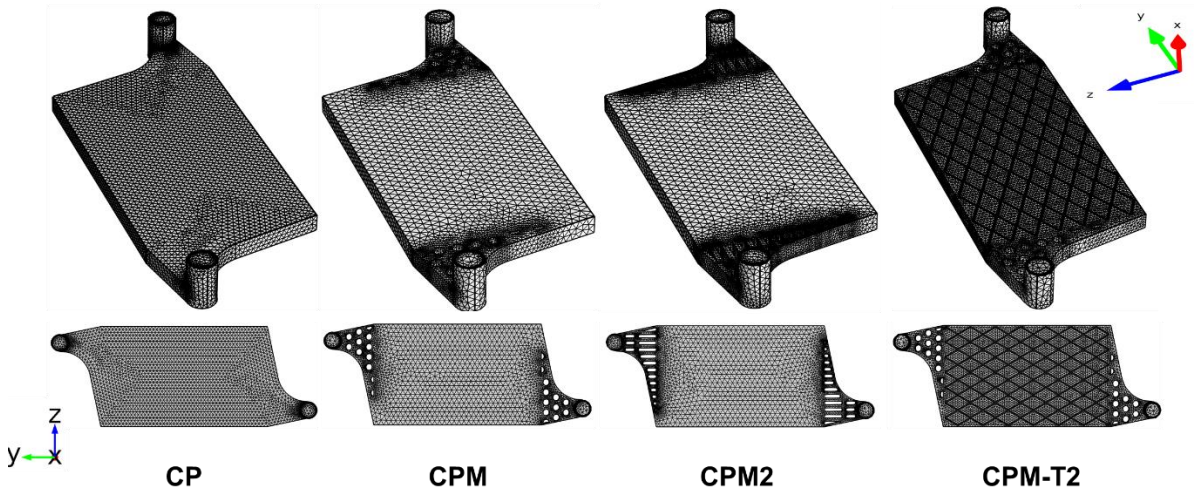

Figure S4. Simulation domains used in CFD studies.

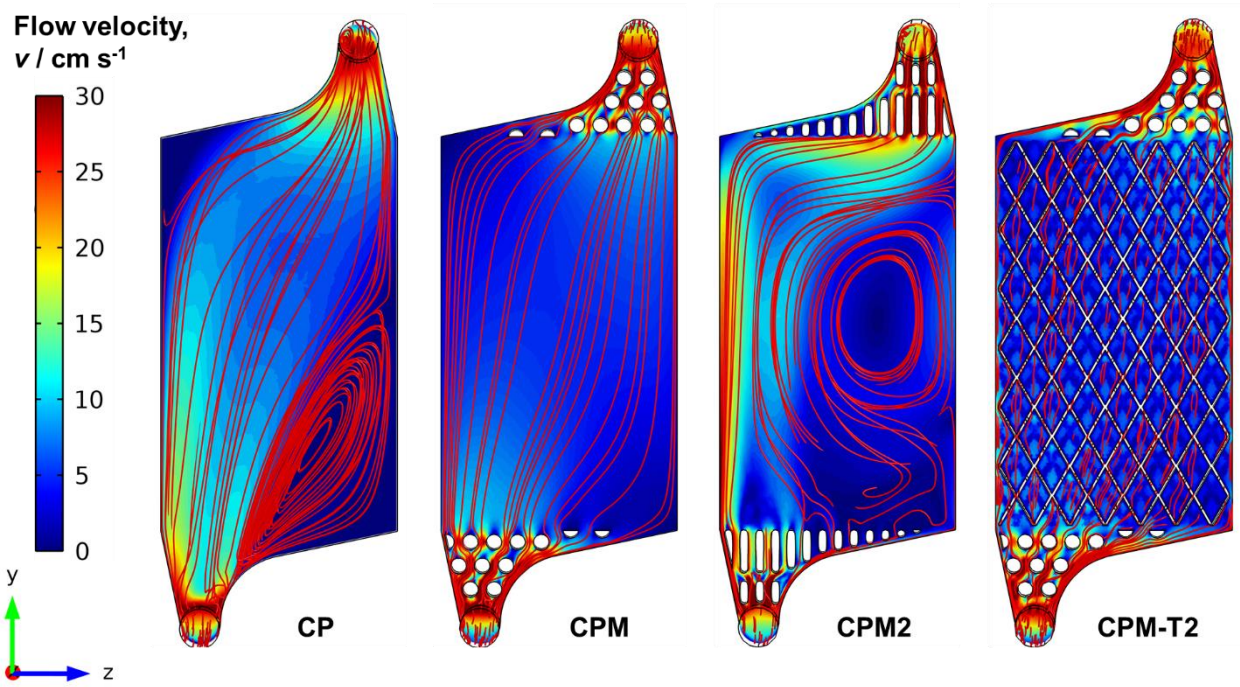

Figure S5. Velocity contour plots and streamlines of simulated configurations at 15 L•h^{-1}.

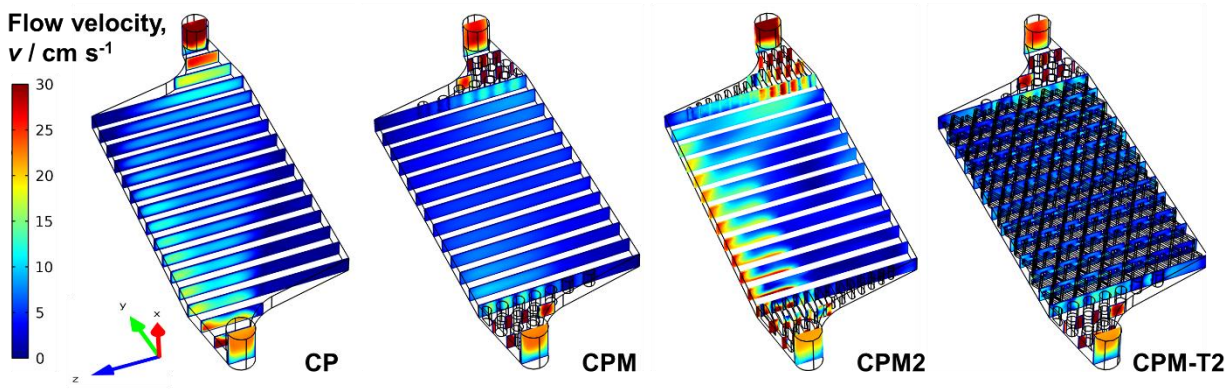

Figure S6. Velocity cross-section planes of simulated configurations at 15 L•h^{-1}.

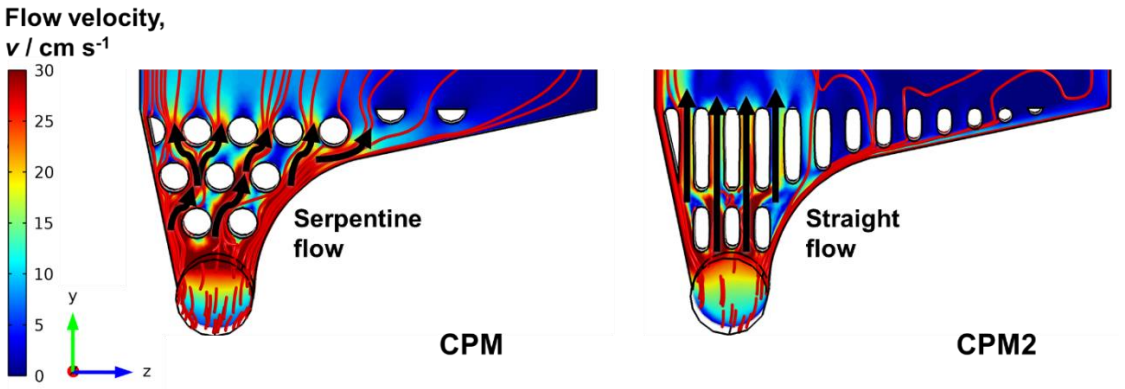

Figure S7. Close-up for visualization of flow patterns in CPM and CPM2 configurations.

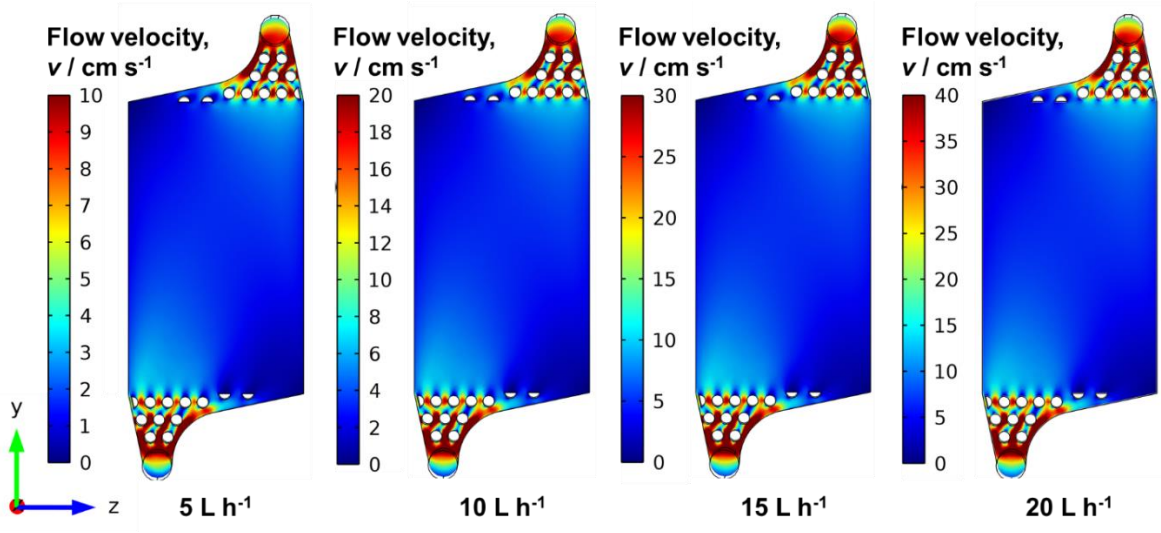

Figure S8. Velocity contour plots of CPM configuration at different flow rates.

5. Flow Visualization.

Recorded dye injections at 15 $L \cdot h^{-1}$ are shown in the supporting information as external files. File No. 1 displays the manifold effect between configurations CP, CPM and CPM2. File No. 2 compares configurations CPM-T1, CPM-T2, CPM-T3 and CPM-NF.

6. Axial-dispersion Model (ADM) for RTD.

A closed-vessel condition was assumed, in which perfect plug-flow occurs before the inlet and after the outlet, and dispersion only occurs inside the vessel.[4] First, the normalized concentration was obtained by means of eq S8:

$$E(\theta) = \frac{c_t}{\int_0^\infty c_t \, dt} \tag{S8}$$

where $E(\theta)$ is the normalized dimensionless concentration and c_t is the tracer concentration at the outlet at time t. Then, experimental residence time τ, and normalized time θ, were calculated by using of eqs S9 and S10, respectively:

$$\tau = \frac{\int_0^\infty t \, c_t \, dt}{\int_0^\infty c_t \, dt} \tag{S9}$$

$$q = \frac{t}{t} \tag{S10}$$

The Péclet number was obtained by fitting eq S11 into experimental $E(\theta)$ against θ curves:

$$E(q) = \frac{\sqrt{Pe}}{4pq^3} \exp\left[- \frac{Pe(1 - q)^2}{4q} \right] \tag{S11}$$

It has been found that this model adequately represents the high levels of dispersion in a closed vessel.[4] The OriginPro® 2016 software package was used to integrate the area under the curves in eqs S8 and S9, as well as to perform the non-linear curve fitting of eq S11. In the latter, an explicit exponential function was created, and Pe was calculated by minimizing the deviations of the theoretical curve from the experimental points using a non-linear least-squares algorithm. Agreement between the fitted model and experimental curves was assessed by means of eq S12:[4]

$$\%\mathrm{Err} = \frac{\int_0^{\infty} \left| E(\theta)_{\mathrm{mod}} - E(\theta)_{\mathrm{exp}} \right| \mathrm{dt}}{\int_0^{\infty} \left| E(\theta)_{\mathrm{mod}} \right| \mathrm{dt}} \times 100 \tag{S12}$$

As a comparison, the dimensionless hold-up ratio was estimated for each RTD curve as follows:

$$j = \left(\frac{t_p}{t} \right) \tag{S13}$$

where t_p is the time for the RTD curve peak (*i.e.*, maximum concentration time). Values of φ close to one are indicative of a fast and uniform evacuation of the electrolyte, with low tailing effects (*i.e.*, there is no stagnant zones that increase the residence time of the electrolyte) .[5]

7. Electrodeposition of Nickel on Stainless Steel Current Collectors

A power supply (BK Precision© 1715A) was used to apply nickel coatings at a constant current (*i.e.*, galvanostatically). A four-step procedure was adapted from previous studies.[6, 7] The steps are as follows: (1) immersion in 37 wt% HCl during 180 s to remove surface oxides, (2) anodic-degreasing in 40 wt% NaOH for 300 s followed by cathodic cleaning at 15 $mA \cdot cm^{-2}$ for 60 s in the same solution, (3) electrodeposition of a thin layer of Ni using a Woods strike bath (120 $mL \cdot L^{-1}$ of 37 wt% HCl and 240 $g \cdot L^{-1}$ of $NiCl_2$) at -70 $mA \cdot cm^{-2}$ for 90 s and (4) electrodeposition of Ni using a Watts bath (260 $g \cdot L^{-1}$ $NiSO_4$, 50 $g \cdot L^{-1}$ $NiCl_2$ and 30 $g \cdot L^{-1}$ of H_3BO_3) at -60 $mA \cdot cm^{-2}$ for 300 s.

All chemicals were purchased from Alfa Aesar®, United States. Fresh solutions were prepared before use. A Ni plate sacrificial anode (Polymet Galvanotech®, 99.8% purity, 0.8 × 50 × 150 mm) was used. During electrodeposition, the exposed geometrical area of each stainless-steel current collector was 35 cm^2. Separation between the electrodes was constant at 3 cm.

8. Complementary RTD results.

Table S2. Experimental values of residence time distribution over the electrochemical reactor.

Configuration	Flow rate ($L \cdot h^{-1}$)	v ($cm \cdot s^{-1}$)	τ (s)	t_p (s)	φ	Pe	D_{ax} (10^4 $m^2 \cdot s^{-1}$)
CP	8	2.116	9.96	3.90	0.39	3.69	2.96
	12	3.175	6.30	2.65	0.42	3.99	4.02
	16	4.233	4.79	2.50	0.52	4.13	5.13
	20	5.291	4.95	2.80	0.57	4.23	6.27
CPM	8	2.116	6.69	3.30	0.49	4.01	2.64
	12	3.175	4.97	3.10	0.62	4.56	3.48
	16	4.233	3.51	2.20	0.63	5.07	4.18
	20	5.291	4.36	2.60	0.60	5.83	4.54
CPM2	8	2.116	4.11	2.59	0.63	3.54	3.17
	12	3.175	3.30	1.83	0.56	3.92	4.11
	16	4.233	2.78	1.56	0.56	4.42	4.82
	20	5.291	3.60	1.78	0.49	4.87	5.47
CPM-T1	8	2.116	5.11	2.68	0.52	4.86	3.36
	12	3.175	4.16	2.37	0.57	5.70	4.3
	16	4.233	2.07	1.26	0.61	5.93	5.49
	20	5.291	2.15	1.31	0.61	6.47	6.33
CPM-T2	8	2.116	5.92	2.86	0.48	4.23	3.09
	12	3.175	5.23	2.55	0.49	4.92	3.99
	16	4.233	2.23	1.34	0.60	6.10	4.29
	20	5.291	2.24	1.59	0.71	6.74	4.85
CPM-T3	8	2.116	9.10	3.10	0.34	2.47	6.79
	12	3.175	5.55	2.70	0.49	3.81	6.41
	16	4.233	4.52	2.10	0.46	4.61	7.08
	20	5.291	4.50	2.40	0.53	5.66	7.20
CPM-NF	8	2.116	5.65	3.50	0.62	4.94	2.22
	12	3.175	3.23	2.80	0.87	6.35	2.58
	16	4.233	2.84	2.45	0.86	7.04	3.10
	20	5.291	2.29	2.14	0.94	8.21	3.33

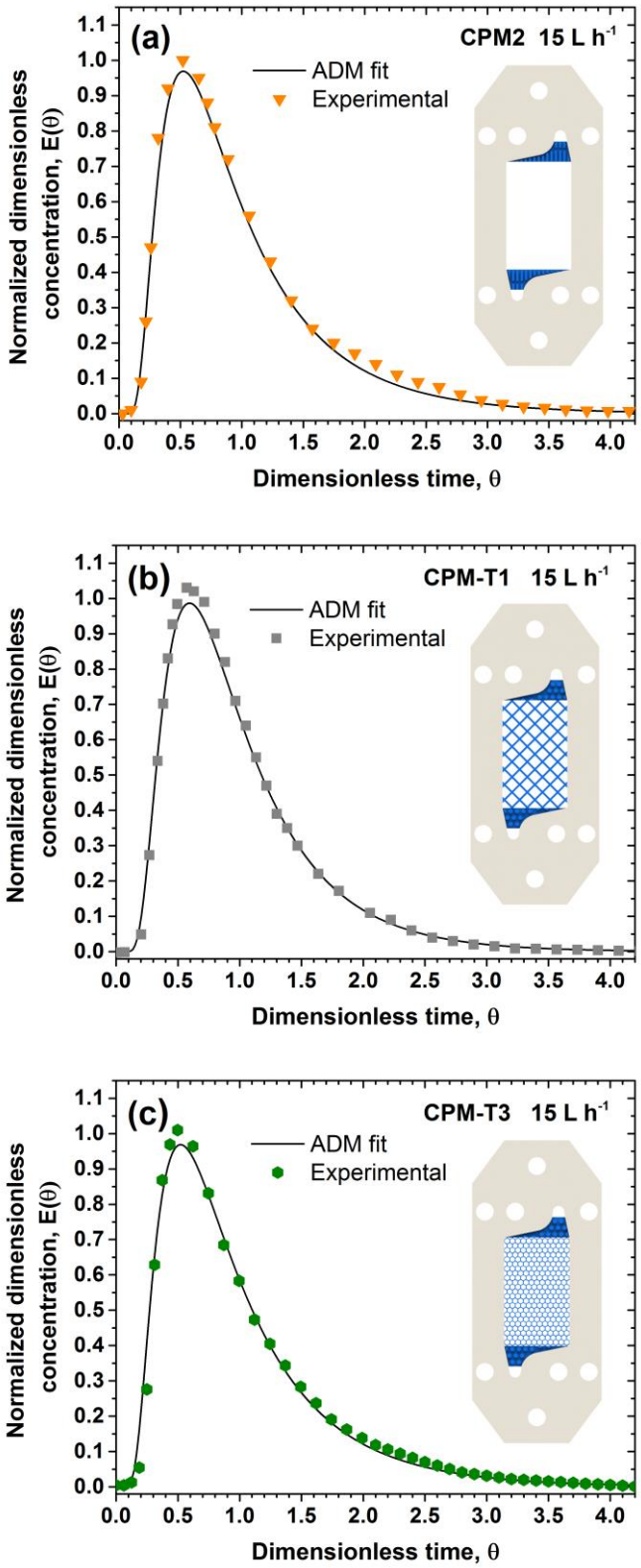

Figure S9. Additional RTD curves for (a) overlapped manifold, (b) square turbulence promoter and (c) hexagonal turbulence promoter. Note: experimental readings in RTD curves do not represent error bars.

9. Coefficients for pressure drop correlation

Table S3. Coefficients of the pressure drop correlation (eq 4) and pressure drop at the nominal design value for different channel configurations.

Configuration	**α (10^2 Pa)**	**β**	**Δp at Re = 175 (Pa)**
CP	0.128	2.19	99.4
CPM	72.73	1.26	458.3
CPM2	20.73	1.53	544.2
CPM-T1	18.33	1.45	321.7
CPM-T2	7.17	1.69	449.5
CPM-T3	5.27	1.71	411.3
CPM-NF	9.11	1.74	776.7

10. Dimensionless Correlations for Mass Transfer Studies on Nickel Electrodes

The product of the mass transfer coefficient and active electrode area, k_mA, were calculated from the limiting current values as follows:[7]

$$k_m A = \frac{I_L}{nFc_b} \tag{S14}$$

where I_L is the limiting current and c_b is the bulk concentration of electroactive species. Then, the mass transfer to a planar electrode was estimated according to the following correlation:[7]

$$Sh = aRe^b Sc^{0.33} L_e^{0.33} \tag{S15}$$

where *Re*, *Sh*, *Sc* and L_e are the Reynolds number, the Sherwood number, the Schmidt number, and the dimensionless length, respectively, and defined as follows:[7, 8]

$$Re = \frac{ud_e}{\in \nu} \tag{S16}$$

$$Sc = \frac{n}{D} \tag{S17}$$

$$Sh = \frac{k_m d_e}{D} \tag{S18}$$

$$L_e = \frac{d_e}{L} \tag{S19}$$

where $d_e = 2BS/(B + S)$ is the equivalent diameter, S is the electrode-membrane gap, B is the width of the channel, ν is the kinematic viscosity of the electrolyte, and D is the diffusion coefficient.

In the case of 3D Ni foam (*i.e.*, CPM-NF configuration) the volumetric mass transfer coefficient was estimated:[6]

$$k_m A_e = \frac{I_L}{nFc_b V_e} \quad \text{(S20)}$$

where A_e is the electrode area per unit volume and V_e is the electrode volume in the flow channel. Subsequently, the dimensionless mass transfer correlation for 3D, porous electrodes was used:[9]

$$Sh = aRe^b Sc^{0.33} \quad \text{(S21)}$$

Furthermore, mass transfer improvement was assessed by the enhancement factor, which is defined as follows:[7]

$$g = \frac{(k_m A)_{enhanced}}{(k_m A)_{empty}} \quad \text{(S22)}$$

where $(k_m A)_{empty}$ refers to the mass transfer coefficient obtained in CPM configuration and $(k_m A)_{enhanced}$ refers to the mass transfer coefficient calculated in configurations with turbulence promoters or Ni foam.

Table S4. Coefficients of dimensionless correlations for different channel configurations.

Configuration	a	b	Ref.
Ni electrode in an open channel	0.39	0.63	10
Ni electrode with TP	5.57	0.40	10
Ni electrode in the FM01-LC reactor with open channel	0.22	0.71	11
Ni electrode in the FM01-LC reactor with TP	0.74	0.62	11
Ni electrode in a 3D-printed flow channel	1.22	0.65	12
CPM (empty channel with non-overlapped manifold)	0.72	0.66	This work
CPM-T1 (square-shaped 3D-printed TP)	1.74	0.68	This work
CPM-T2 (diamond-shaped 3D-printed TP)	1.88	0.61	This work
CPM-T3 (hexagonal-shaped 3D-printed TP)	0.78	0.69	This work
CPM-NF (Ni foam 3D electrode)	1.11	0.78	This work

TP: turbulence promoter

11. Extended nomenclature

A_e	Electrode area per unit volume (m^2 m^{-3})
A_{geo}	Projected geometrical electrode area (m^2)
a	Geometric coefficient for Sherwood number dimensionless correlation
B	Channel width (m)
b	Hydraulic exponent for Sherwood number dimensionless correlation
c	Concentration (M)
c_b	Bulk concentration (M)
c_t	Tracer concentration at time *t* (M)
D	Diffusion coefficient (m^2 s^{-1})
D_{ax}	Axial dispersion coefficient (m^2 s^{-1})
d_e	Equivalent diameter (m)
E	Electrode potential (V)
$E(\theta)$	Normalized dimensionless concentration
F	Faraday's constant (96,487 A s^{-1} mol^{-1})
I	Current (A)
I_L	Limiting current (A)
k	Turbulent kinetic energy (m^2 s^{-2})
k_m	Mass transfer coefficient (m s^{-1})
L	Length of the flow channel (m)
L_e	Dimensionless length
n	Number of electrons transferred
p	Pressure (Pa)
Pe	Péclet number
Q	Volumetric flow rate (m^3 s^{-1})
Re	Reynolds number
S	Membrane-electrode gap (m)
Sc	Schmidt number
T	Absolute temperature (K)
t	Time (s)
t_p	RTD curve peak time (s)
u	Mean linear velocity of the fluid (m s^{-1})

V_e Electrode volume in the flow channel (m^3)

V_s Copper sensor volume (m^3)

Greek characters

α Coefficient for pressure drop correlation

β Exponent for pressure drop correlation

δ Parameter measured in chemical resistance assessment

ε Turbulent energy dissipation rate ($m^2\ s^{-3}$)

ϵ Porosity

φ Dimensionless hold-up ratio

γ Enhancement factor

μ Dynamic viscosity (Pa s)

μ_T Turbulent viscosity (Pa s)

ν Kinematic viscosity of the solution ($m^2\ s^{-1}$)

ρ Density of the solution ($kg\ m^{-3}$)

θ Normalized time

τ Residence time in the reactor (s)

12. References

(1). Sandoval, M. A.; Fuentes, R.; Walsh, F. C.; Nava, J. L.; de León, C. P., Computational fluid dynamics simulations of single-phase flow in a filter-press flow reactor having a stack of three cells. *Electrochim. Acta* **2016,** *216*, 490-498. https://doi.org/10.1016/j.electacta.2016.09.045

(2). Rivera, F. F.; Castañeda, L.; Hidalgo, P. E.; Orozco, G., Study of Hydrodynamics at AsahiTM prototype electrochemical flow reactor, using computational fluid dynamics and experimental characterization techniques. *Electrochim. Acta* **2017,** *245*, 107-117. https://doi.org/10.1016/j.electacta.2017.05.134

(3). Rivero, E. P.; Cruz-Díaz, M. R.; Almazán-Ruiz, F. J.; González, I., Modeling the effect of non-ideal flow pattern on tertiary current distribution in a filter-press-type electrochemical reactor for copper recovery. *Chem. Eng. Res. Des.* **2015,** *100*, 422-433. https://doi.org/10.1016/j.cherd.2015.04.036

(4). Trinidad, P.; Ponce de León, C.; Walsh, F. C., The application of flow dispersion models to the FM01-LC laboratory filter-press reactor. *Electrochim. Acta* **2006,** *52*, (2), 604-613. https://doi.org/10.1016/j.electacta.2006.05.040

(5). Rivera, F. F.; Cruz-Díaz, M. R.; Rivero, E. P.; González, I., Analysis and interpretation of residence time distribution experimental curves in FM01-LC reactor using axial dispersion and plug dispersion exchange models with closed–closed boundary conditions. *Electrochim. Acta* **2010,** *56*, (1), 361-371. https://doi.org/10.1016/j.electacta.2010.08.069

(6). Arenas, L. F.; Ponce de León, C.; Walsh, F. C., 3D-printed porous electrodes for advanced electrochemical flow reactors: A Ni/stainless steel electrode and its mass transport characteristics. *Electrochem. Commun.* **2017,** *77*, 133-137. https://doi.org/10.1016/j.elecom.2017.03.009

(7). Recio, F. J.; Herrasti, P.; Vazquez, L.; Ponce de León, C.; Walsh, F. C., Mass transfer to a nanostructured nickel electrodeposit of high surface area in a rectangular flow channel. *Electrochim. Acta* **2013,** *90*, 507-513. https://doi.org/10.1016/j.electacta.2012.11.135

(8). Cañizares, P.; García-Gómez, J.; Fernández de Marcos, I.; Rodrigo, M. A.; Lobato, J., Measurement of Mass-Transfer Coefficients by an Electrochemical Technique. *J. Chem. Educ.* **2006,** *83*, (8), 1204-1207. https://doi.org/10.1021/ed083p1204

(9). Arenas, L. F.; Ponce de León, C.; Walsh, F. C., Engineering aspects of the design, construction and performance of modular redox flow batteries for energy storage. *J. Energy Storage* **2017,** *11*, 119-153. https://doi.org/10.1016/j.est.2017.02.007

(10). Carlsson, L.; Sandegren, B.; Simonsson, D.; Rihovsky, M., Design And Performance Of A Modular, Multi-Purpose Electrochemical Reactor. *J. Electrochem. Soc.* **1983,** *130*, (2), 342-346. https://doi.org/10.1149/1.2119708

(11). Brown, C. J.; Pletcher, D.; Walsh, F. C.; Hammond, J. K.; Robinson, D., Studies of space-averaged mass transport in the FM01-LC laboratory electrolyser. *J. Appl. Electrochem.* **1993,** *23*, (1), 38-43. https://doi.org/10.1007/BF00241573

(12). Ponce De Leon, C.; Hussey, W.; Frazao, F.; Jones, D.; Ruggeri, E.; Tzortzatos, S.; McKerracher, R. D.; Wills, R. G. A.; Yang, S.; Walsh, F. C., The 3D printing of a polymeric electrochemical cell body and its characterisation. *Chem. Eng. Trans.* **2014,** *41*, (Special Issue), 1-6. https://doi.org/10.3303/CET1441001